www.sciencemag.org/cgi/content/full/320/5876/626/DC1

Supporting Online Material for

Structure and Dynamics of Earth's Lower Mantle

Edward J. Garnero* and Allen K. McNamara

*To whom correspondence should be addressed. E-mail: garnero@asu.edu

Published 2 May 2008, *Science* **320**, 626 (2008)
DOI: 10.1126/science.1148028

This PDF file includes:

SOM Text

Figs. S1 to S5

Table S1

References

Fig. 1 in the main text displays a number of D″ phenomena imaged by seismic methods. These findings are summarized in the graphical table (Fig. S1), and emphasize that the D″ region represents a significant level of complexities in comparison with the overlying lower mantle.

Information regarding Fig. 2 in the main text

Fig. 2A in the main text displays seismic tomography model S20RTS (*S1, S2*) at the resolution of degree 20. Only anomalies beneath 660 km depth are shown. Red and blue iso-surfaces represent contours of -0.6% and 0.6%, respectively.

The main text presents geodynamic modeling of thermochemical structures. An additional possibility to explain the large low shear velocity provinces (LLSVPs) includes clusters of smaller plumes, either isochemical or thermochemical (Fig. S2). Numerical convection experiments indicate that large thermal megaplumes are not observed in isochemical convection calculations, indicating they are unlikely explanations of the LLSVPs (*S3, S4*). Thermal plume clusters, however, are dynamically feasible (*S4, S5*) and possibly compatible with long wavelength tomographic images, where resolution limitations may blur such features into larger apparent anomalies (*S6*). Both of these possibilities, however, are inadequate in explaining elevated LLSVP density, and sharp LLSVP edges.

For thermochemical structures, both temperature and composition are included in the dynamical buoyancy forces. These structures are significantly hotter than surrounding mantle, largely because heat loss is inhibited by a conductive thermal boundary layer that forms along their surfaces. Seismic imaging only characterizes present day LLSVP shape, and it is therefore instructive to consider the temporal evolution of thermochemical structures, which depends critically on effective density, defined as intrinsic density minus the density reduction due to thermal expansion.

Geodynamical calculations in Fig 2 of the main text are results that were performed to illustrate the various conceptual models hypothesized to explain the presence of the LLSVPs observed from seismology beneath Africa and the Pacific. Calculations shown in main text Fig. 2(B,C) and Fig. S2B below were performed using the thermochemical extension of CitcomS (*S7, S8*). The calculations shown in Fig. 2(D) and Fig. S2(C) were performed using the 2D Cartesian Citcom code with the addition of tracers (*S9, S10*). The 3 dimensional calculations are performed in a spherical geometry, and final temperature and composition fields are unwrapped into a Cartesian geometry as a post processing step to enhance visualization. Calculations utilize the ratio tracer method to carry out the advection of composition, as described and tested by (*S11*). The calculations leading to isochemical plume clusters and thermochemical piles utilize observed plate motions for the past 119 million years as surface boundary conditions (*S12*), as used in (*S13*). The other calculations do not include plate motions.

The calculations use the finite element method to solve the non-dimensionalized conservation equations of mass, momentum, and energy using the Boussinesq approximation.

$$\nabla \cdot \mathrm{u} = 0$$

$$-\nabla P + \nabla \cdot (\eta \dot{\varepsilon}) = (RaT - RbC)\hat{\mathrm{r}}$$

$$\frac{\partial T}{\partial t} + (\mathrm{u} \cdot \nabla) T = (\nabla^2 T) + \mathrm{H}$$

Unless otherwise noted, all variables are non-dimensional where **u** is the velocity, P is the dynamic pressure, η is the viscosity, $\dot{\varepsilon}$ is the strain rate tensor, Ra is the thermal Rayleigh number, T is the temperature, Rb is the chemical Rayleigh number, C is the composition, t is time, and H is the internal heating rate.

$$Ra = \frac{\rho g \alpha \Delta \mathrm{T} h^3}{\eta_o \kappa_o}$$

$$Rb = \frac{\Delta \rho g h^3}{\eta_o \kappa_o}$$

The Rayleigh numbers are defined above, and are a collection of the following dimensional constants: ρ is density, g is the acceleration of gravity, α is thermal expansivity, ΔT is the temperature contrast between surface and bottom of the mantle, h is the mantle thickness, η_o is the reference viscosity, κ_o is the diffusivity, and $\Delta\rho$ is the intrinsic density contrast between more-dense material and the surrounding mantle. Thermochemical calculations may be defined by their Buoyancy Number, B, which is a measure of compositional over thermal forces:

$$B = \frac{Rb}{Ra} = \frac{\Delta\rho}{\rho\alpha\Delta \mathrm{T}} \quad .$$

Rheology is temperature-dependent, defined by:

$$\eta(T) = \eta_r \exp\left[A(0.5 - T)\right] \ ,$$

where A is the activation coefficient that controls the temperature dependence, and η_r is the viscosity prefactor.

Parameters for the geodynamical calculations are given in the following table:

Calculation	Fig.	Ra	B	A	η_r	Initial thermochemical configuration	other	Inspired by (*ref*)
Thermochemical Piles	Main text: 2B, Suppl. Fig S4B	1.4×10^8	0.6	9.21	1 in upper mantle; 30-300 linearly increasing in lower mantle	Flat 255 km layer	Includes plate motions for past 119 Ma	(*13,17*)
Thermochemical Superplumes	Main text: 2C	4.7×10^6	0.4	6.91	1	Flat 510 km layer	Plate motions are not included	(*S15,S16*)
Transient Piles (created by subducted crust)	Main text: 2D	5×10^7	0.8	9.21	1 in upper mantle; 50 in lower mantle	10 km continuously forming layer at surface	-	(*S18-S21*)
Isochemical Plume Clusters	Suppl. Fig S2B, S4A	1.4×10^8	NA	9.21	1 in upper mantle; 30-300 linearly increasing in lower mantle	NA	Includes plate motions for past 119 Ma	(*S14*)
Thermochemical Plume Clusters	Suppl. Fig S2C	5.0×10^7	0.7	9.21	1 in upper mantle; 50 in lower mantle	5 km continuously forming layer at the CMB	-	-

Discussion regarding anisotropy and the perovskite to post-perovskite phase transition

Fig. S3 schematically illustrates 4 possible scenarios regarding the formation of lattice preferred orientation (LPO)-induced seismic anisotropy due to magnesiowüstite [(Mg,Fe)O], perovskite, and post-perovskite. Panels on the left side of the Fig. illustrate simplified dynamics of subducted material deforming as it reaches the lowermost mantle and is forced to flow laterally due to impacting the CMB. The dashed horizontal line represents the perovskite-to-post-perovskite phase transition. Smaller horizontal lines depict strain due to the expected horizontal pure shear stretching (*S22,S23*). Strain lines shown in green, blue, and red represent strain, hence LPO formation, in perovskite, post-perovskite, and magnesiowüstite, respectively. Panels to the right of each dynamical cartoon show the expected magnitude of LPO formation, hence some measure of seismic anisotropy, with depth in a qualitative, schematic manner.

Fig. S3(A) represents a scenario in which both perovskite and post-perovskite cause LPO-induced seismic anisotropy. Above the phase transition, LPO begins to form in perovskite due to horizontal stretching. At further depths however, as perovskite transforms to post-perovskite, the large change in crystalline structure might destroy any pre-existing LPO. It takes a finite amount of subsequent deformation, occurring deeper than the phase transition, to develop new LPO which may lead to anisotropy. If this is occurring, we expect to see seismic anisotropy throughout the D″ region, except for a layer directly beneath the transition in which anisotropy is expected to be absent. Future joint mineral physics, geodynamics, and seismological studies are required to determine how thick this layer would actually be.

Fig. S3(B) represents a scenario similar to that shown in Fig. S3(A) except that the only LPO producing mineral is post-perovskite. If this is the case, we expect to see seismic anisotropy only in the deepest regions of the mantle, at some finite depth below the phase transition.

Fig.s S3(C) and S3(D) represent more general, but perhaps more-realistic scenarios. These combine the scenarios of Fig.s S3(A) and S3(B) with the possibility of magnesiowüstite also causing LPO (*S24*). LPO developed in magnesiowüstite is not expected to be affected by the post-perovskite phase transition, and hence may gradually increase with depth, starting above the transition. In the lowermost mantle, superimposed upon the magnesiowüstite LPO is that caused by post-perovskite, developing well-beneath the phase transition. In general, we do not expect the fast directions of seismic anisotropy to be correlated in these 2 minerals. Furthermore, it is critically important to access which of the two minerals (magnesiowüstite or post-perovskite) is rheologically weaker. It is conceivable that the weaker of the two will accommodate the most deformation, hence create the strongest LPO. Mineral physics research continues to advance our understanding of the nature of the post-perovskite phase (*S*25-*S*35), which is a necessary step in refinement of our abilities to connect the seismic anisotropy models to deep mantle flow.

Basal mantle temperatures and ULVZ locations

As discussed in the main text, ULVZs may be preferentially located in the hottest regions of the deepest mantle. Fig. S4, below, shows the temperature distribution for an isochemical and thermochemical convection calculation (see Table, above). In the case of isochemical convection, highest temperatures are in the center of warm areas, beneath plumes; in thermochemical convection, highest temperatures are near pile edges. Therefore, seismic mapping of ULVZ structure holds promise in improving constraint on large scale deep mantle chemistry, particularly if the LLSVPs in the deep mantle are due to piles or not (the similarity is shown in Fig. S5).

Supplementary Fig. captions

Fig. S1. Vertical scale lengths of seismically imaged lowermost mantle phenomena: large low shear velocity province (LLSVP), D″ discontinuity, ultra-low velocity zone (ULVZ), D″ anisotropy, and scatterers. The D″ region is defined as the lowermost mantle depth shell that contains these phenomena.

Fig. S2. (A), as Fig. 2A in main text: tomographically derived (*S2*) high and low seismic shear velocity variations in Earth's mantle (blue and red, respectively) are shown below 660 km depth. All panels are for the entire depth range of the mantle. (B) Plume clusters for an 3D isochemical convection calculation. (C) Multiple plumes in an upwelling region for a 2D geodynamical calculation with unique D" chemistry.

Fig. S3: Schematic images illustrating how the minerals magnesiowüstite, perovskite, and post-perovskite may lead to complex patterns of lattice preferred orientation (LPO), hence seismic anisotropy. Panels on the left show simplified dynamics of a slab impinging upon the core-mantle boundary (CMB). Green, blue, and red line segments represent LPO formation due to strain in perovskite, post-perovskite, and magnesiowüstite, respectively. The horizontal dashed line represents the pos-perovskite phase transition. Panels to the right represent qualitative magnitude of fabric development for each of the minerals with depth. Cases are shown in which (A) only perovskite and post-perovskite, (B) post-perovskite, (C) magnesiowüstite and post-perovskite, and (D) magnesiowüstite, perovskite, and post-perovskite contribute to seismic anisotropy.

Fig. S4: Temperature maps at lowermost mantle depths are shown for geodynamical calculations that lead to (A) isochemical plume clusters and (B) thermochemical piles. Depth of the temperature distribution is 20 km above the CMB. These are taken from calculations performed to generate Fig. 2 in the main text. Color represents non-dimensional temperature, with 1 and 0 being the hottest and coldest, respectively. (A) Plume clusters lead to linear hot ridges in map view. In this hypothetical model, ULVZ is expected to follow a pattern similar to these hot linear ridges. (B) Thermochemical piles lead to hot ridges along their perimeter edges as well as some in their interior. Thus each case represents a different pattern of highest mantle temperatures in relationship to the shapes of LLSVPs, and hence implicitly predicts different ULVZ distribution, for ULVZ structure that relates to temperature (e.g., a partial melt origin to ULVZ).

Fig. S5. (**A**) Cross-section displays temperature variations of a thermochemical convection calculation, which has cold (blue) downwellings, and a hot (red) thermochemical pile and plumes that form at pile ridges. This calculation corresponds to Fig. 2B in the main text. (**B**) Cross-section showing seismic shear-wave velocity perturbations from model S20RTS (*S1-S2*).

Supplemental Text References:

S1. J. Ritsema, H. J. van Heijst, J. H. Woodhouse, *Science* **286**, 1925 (1999).
S2. J. Ritsema, H. J. van Heist, J. H. Woodhouse, *J. Geophys. Res.*, **109**, doi:10.1029/2003JB002610, B02302 (2004).
S3. H.-P. Bunge, M. A. Richards, C. Lithgow-Bertelloni, J. R. Baumgardner, S. P. Grand, and B. A. Romanowicz, *Science* **280**, 91 (1998).
S4. A. K., McNamara, S. Zhong, *Nature* **437**, 1136 (2005).
S5. G. Schubert, G. Masters, P. Olson, P. Tackley, *Phys. Earth Planet. Int*. **146**, 147 (2004).
S6. J. Ritsema, A. K. McNamara, A. L. Bull, *J. Geophys. Res*. **112**, doi:10.1029/2006JB004566, B01303 (2007).
S7. S. Zhong, M. T. Zuber, L. Moresi, M. Gurnis, *J. Geophys. Res.* **105**, 11063 (2000).
S8. A. K. McNamara, S. Zhong, *J. Geophys. Res.* **109**, doi:10.1029/2003JB/2003JB002847, B07402 (2004).
S9. L. Moresi, M. Gurnis, *Earth Planet. Sci. Lett.* **138**, 15 (1996).
S10. A. K. McNamara, S. Zhong, *Earth Planet. Sci. Lett.* **222**, 485 (2004).
S11. P. J. Tackley, S. D. King, *Geochem., Geophys. Geosyst*. **4** doi:10.1029/2001GC000214 (2003).
S12. C. Lithgow-Bertelloni, M. A. Richards, *Rev. Geophys.* **36**, 27 (1998).
S13. A. K. McNamara, S. Zhong, *Nature* **437**, 1136 (2005).
S14. G. Schubert, G. Masters, P. Olson, P. Tackley, *Phys. Earth Planet. Int.* **146**, 147 (2004).
S15. A. Davaille, Nature 402, 756 (1999).
S16. A. Davaille, E. Stutzmann, G. Silveira, J. Besse, V. Courtillot, *Earth Planet. Sci. Lett.* **239**, 233 (2005).
S17. P. J. Tackley, *Geochem., Geophys. Geosyst.* **3**, doi:10.1029/2001GC000167, 1024 (2002).
S18. U. R. Christensen, A.W. Hofmann, *J. Geophys. Res.* **99**, 19867 (1994).
S19. T. Nakagawa, B. A. Buffett, *Earth Planet. Sci. Lett.* **230**, 11 (2005).
S20. T. Nakagawa, P. J. Tackley, *Earth Planet. Sci. Lett.,* **238**, 204 (2005).
S21. E. Tan, M. Gurnis, *Geophys. Res. Lett.*, **32**, doi:10.1029/2005GL024190, L20307 (2005).
S22. A. K. McNamara, P. E. van Keken, S. Karato, *Nature* **416**, 310 (2002).
S23. A. K. McNamara, P. E. van Keken, S. –I. Karato, *J. Geophys. Res.* **108,** doi:10.1029/2002JB001970, 2230 (2003).
S24. D. Yamazaki, S. Karato, *Phys. Earth Planet. Inter.* **131**, 251 (2002).
S25. F. Zhang, A. R. Oganov, *Earth Planet. Sci. Lett.* **248**, 54 (2006).
S26. S.-H. Shim, A. Kubo, T. S. Duffy, *Earth Planet. Sci. Lett.* **260**, 166 (2007).
S27. M. Murakami, S. V. Sinogeikin, J. D. Bass, N. Sata, Y. Ohishi, K. Hirose, *Earth Planet. Sci. Lett.* **259**, 18 (2007).
S28. T. Yagi, in *Post-perovskite, The Last Mantle Phase Transition*, K. Hirose, J. Brodholt, T. Lay, D. Yuen, Eds. (American Geophysical Union, Washington, D. C., 2007), pp. 9-18.
S29. K. Hirose, in *Post-perovskite, The Last Mantle Phase Transition*, K. Hirose, J. Brodholt, T. Lay, D. Yuen, Eds. (American Geophysical Union, Washington, D. C., 2007), pp. 19-36.
S30. W. Mao *et al,* in *Post-perovskite, The Last Mantle Phase Transition*, K. Hirose, J. Brodholt, T. Lay, D. Yuen, Eds. (American Geophysical Union, Washington, D. C., 2007), pp. 37-46.

S31. J. Li, in *Post-perovskite, The Last Mantle Phase Transition*, K. Hirose, J. Brodholt, T. Lay, D. Yuen, Eds. (American Geophysical Union, Washington, D. C., 2007), pp. 47-68.
S32. D. Yamazaki, S.-i. Karato, in *Post-perovskite, The Last Mantle Phase Transition*, K. Hirose, J. Brodholt, T. Lay, D. Yuen, Eds. (American Geophysical Union, Washington, D. C., 2007), pp. 69-78.
S33. R. M. Wentzcovitch, K. Umemoto, T. Tsuchiya, J. Tsuchiya, in *Post-perovskite, The Last Mantle Phase Transition*, K. Hirose, J. Brodholt, T. Lay, D. Yuen, Eds. (American Geophysical Union, Washington, D. C., 2007), pp. 79-98.
S34. S. Stackhouse, J. P. Brodholt, in *Post-perovskite, The Last Mantle Phase Transition*, K. Hirose, J. Brodholt, T. Lay, D. Yuen, Eds. (American Geophysical Union, Washington, D. C., 2007), pp. 99-114.
S35. R. Caraca, R. E. Cohen, in *Post-perovskite, The Last Mantle Phase Transition*, K. Hirose, J. Brodholt, T. Lay, D. Yuen, Eds. (American Geophysical Union, Washington, D. C., 2007), pp. 115-128.

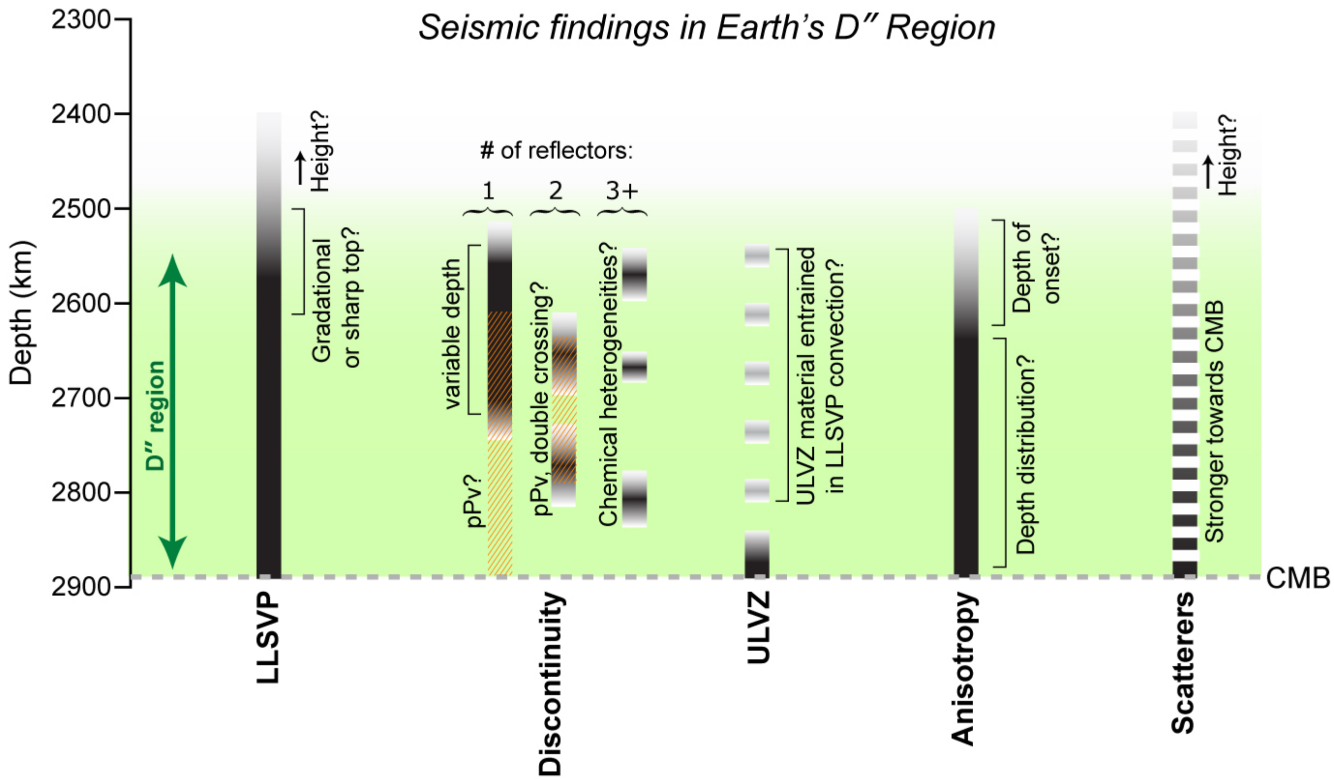

FIGURE S1
Garnero and McNamara (2008)

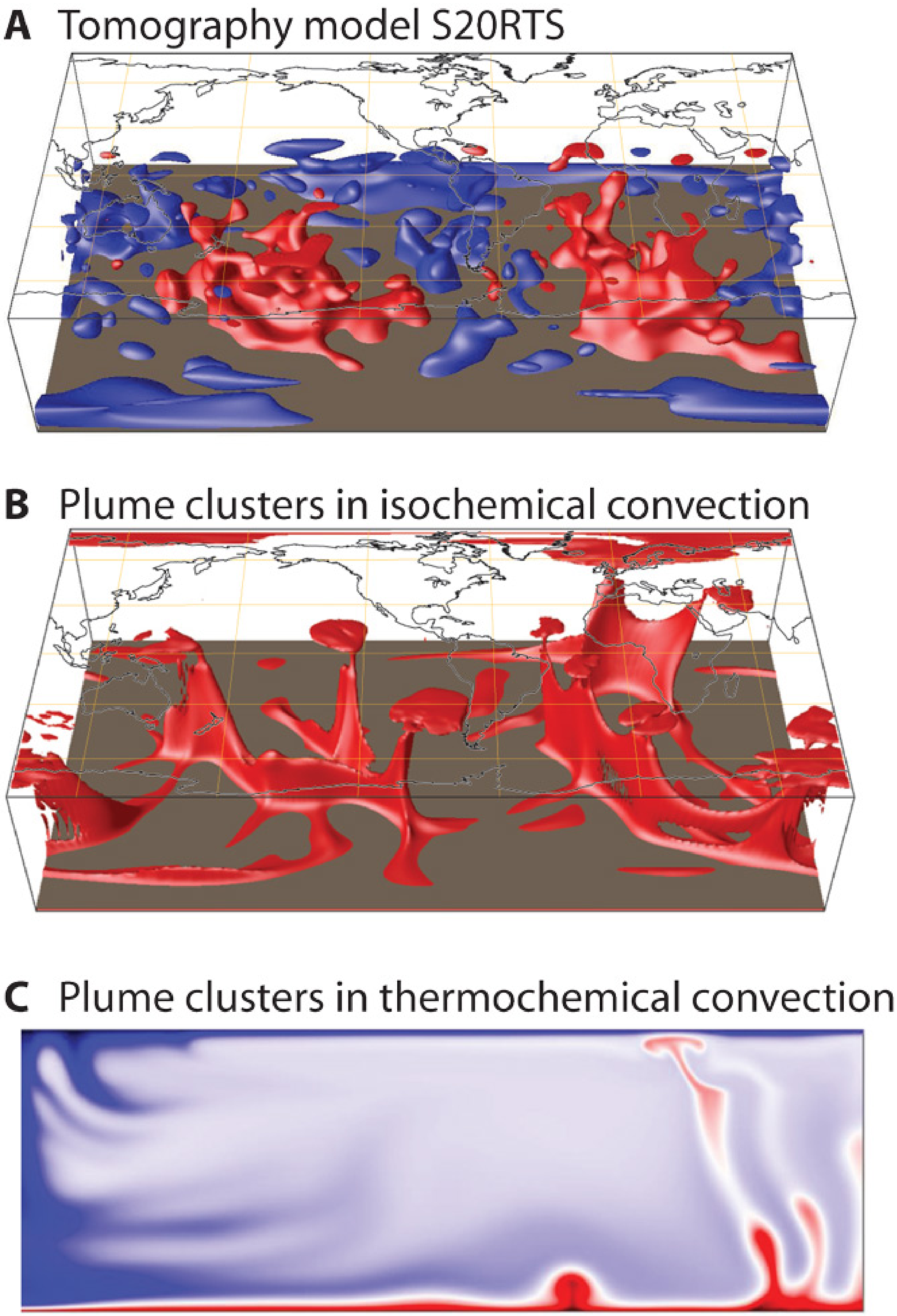

FIGURE S2
Garnero and McNamara (2008)

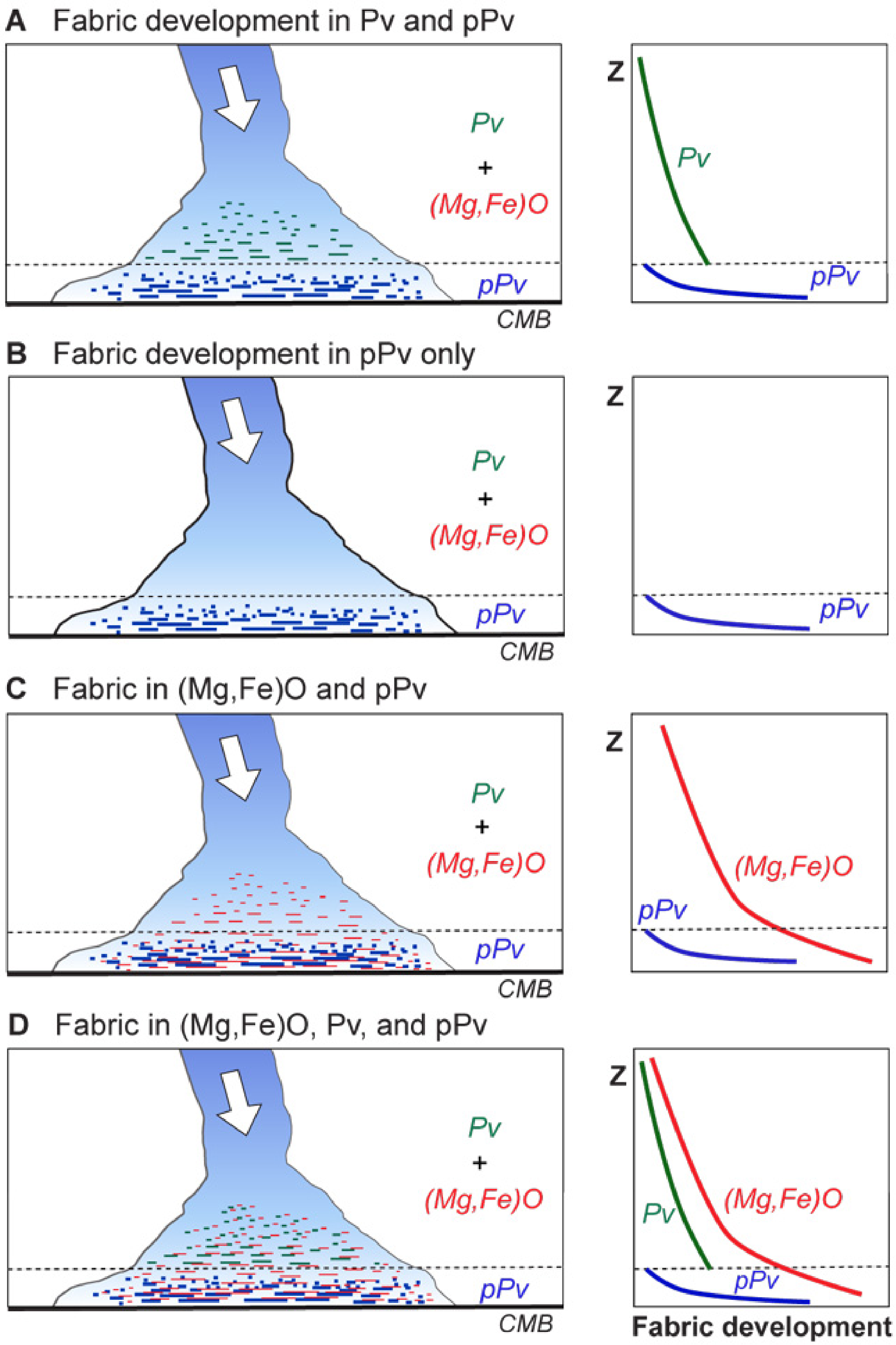

FIGURE S3
Garnero and McNamara (2008)

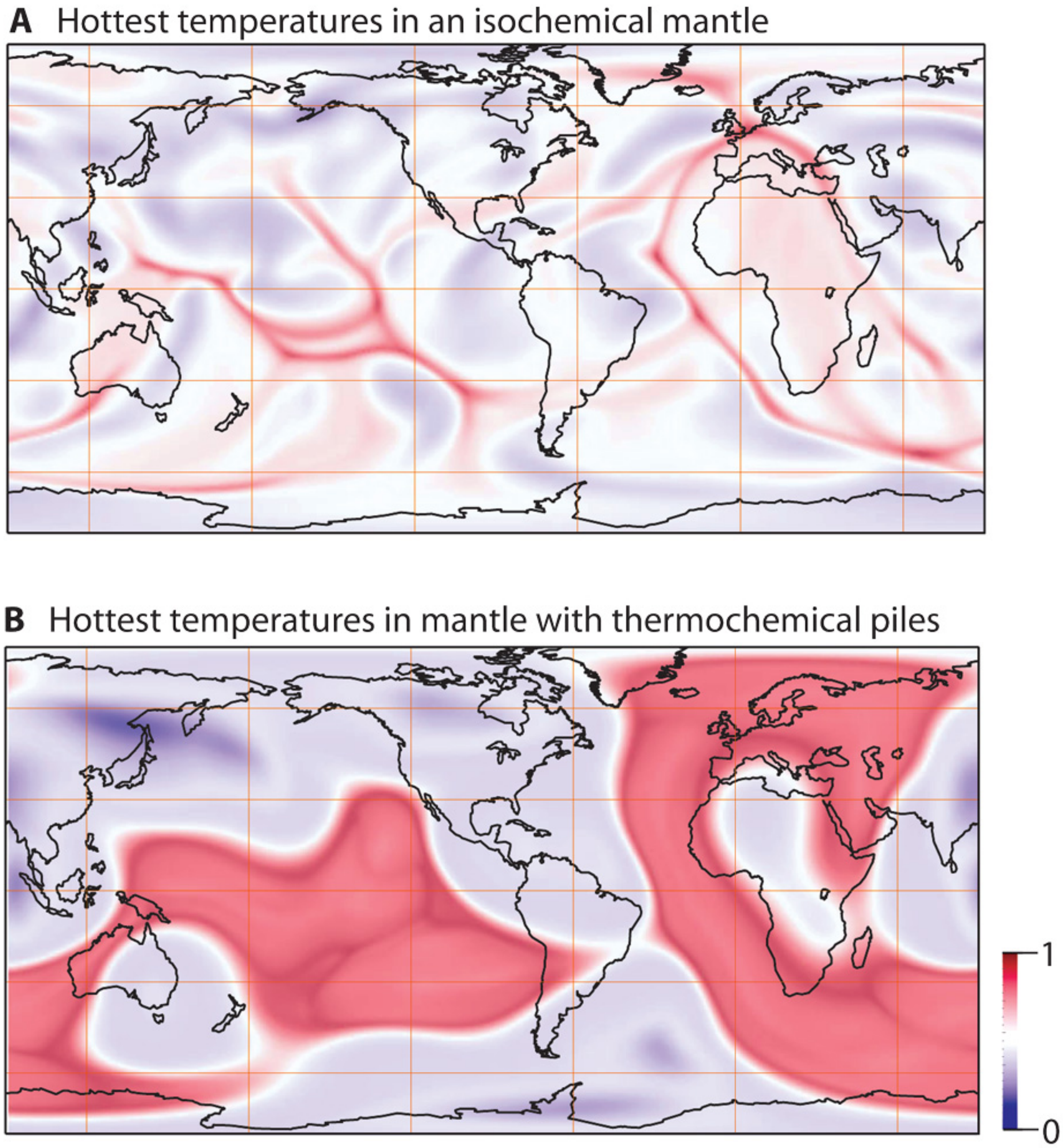

FIGURE S4
Garnero and McNamara (2008)

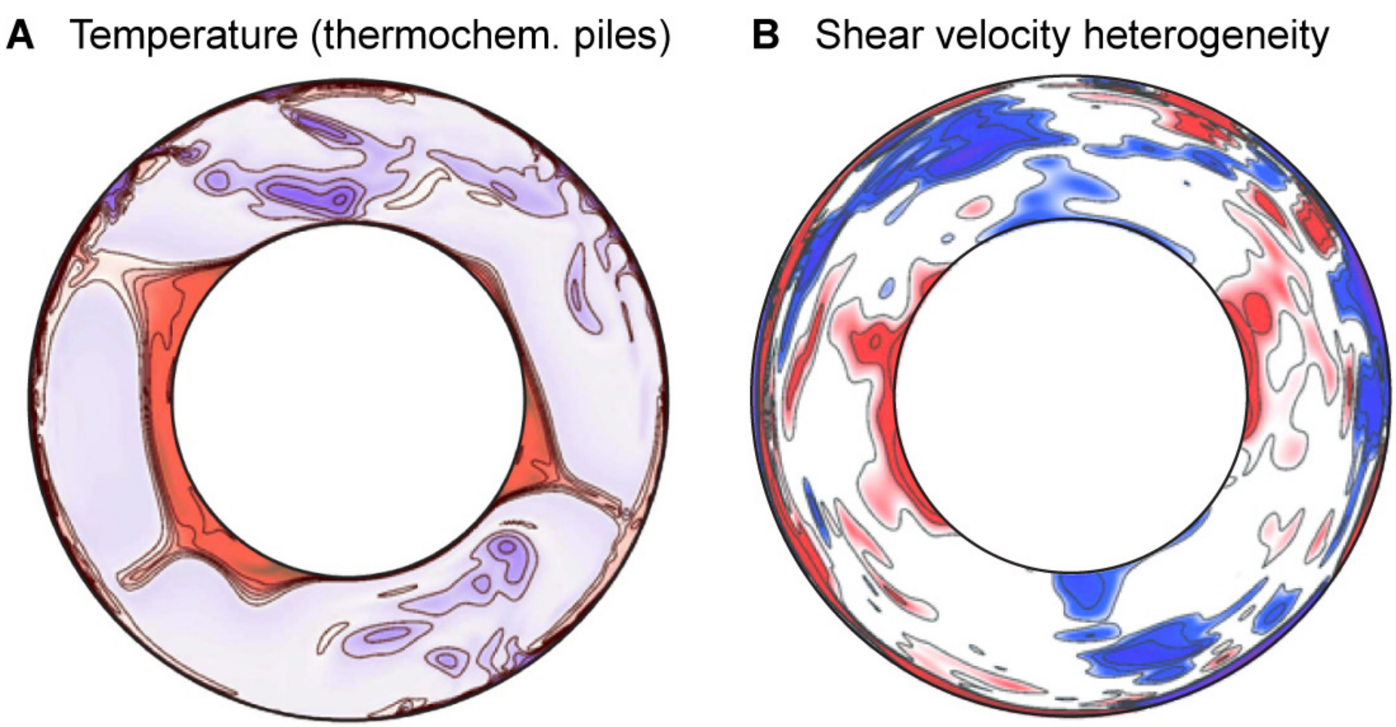

FIGURE S5
Garnero and McNamara (2008)